Journal of
Manufacturing and Materials Processing

MDPI

Article

Fused Filament Fabrication of WC-10Co Hardmetals: A Study on Binder Formulations and Printing Variables

Julián David Rubiano Buitrago [1,*], Andrés Fernando Gil Plazas [2], Luis Alejandro Boyacá Mendivelso [3] and Liz Karen Herrera Quintero [1]

[1] Department of Mechanical and Mechatronics Engineering, Faculty of Engineering, Universidad Nacional de Colombia, Bogotá 111321, Colombia; lkherreraq@unal.edu.co
[2] Materials and Testing Center, Servicio Nacional de Aprendizaje-SENA, Bogotá 111511, Colombia; agilp@sena.edu.co
[3] Department of Chemical and Environmental Engineering, Faculty of Engineering, Universidad Nacional de Colombia, Bogotá 111321, Colombia; laboyacam@unal.edu.co
* Correspondence: judrubianobu@unal.edu.co

Abstract: This research explores the utilization of powder fused filament fabrication (PFFF) for producing tungsten carbide-cobalt (WC-10Co) hardmetals, focusing on binder formulations and their impact on extrusion force as well as the influence of printing variables on the green and sintered density of samples. By examining the interplay between various binder compositions and backbone contents, this study aims to enhance the mechanical properties of the sintered parts while reducing defects inherent in the printing process. Evidence suggests that formulated feedstocks affect the hardness of the sintered hardmetal—not due to microstructural changes but macrostructural responses such as macro defects introduced during printing, debinding, and sintering of samples. The results demonstrate the critical role of polypropylene grafted with maleic anhydride (PP-MA) content in improving part density and sintered hardness, indicating the need for tailored thermal debinding protocols tailored to each feedstock. This study provides insights into feedstock formulation for hardmetal PFFF, proposing a path toward refining manufacturing processes to achieve better quality and performance of 3D printed hardmetal components.

Keywords: hardmetals; powder fused filament fabrication; additive manufacturing; feedstock formulation; printing force measurement

Citation: Rubiano Buitrago, J.D.; Gil Plazas, A.F.; Boyacá Mendivelso, L.A.; Herrera Quintero, L.K. Fused Filament Fabrication of WC-10Co Hardmetals: A Study on Binder Formulations and Printing Variables. *J. Manuf. Mater. Process.* **2024**, *8*, 118. https://doi.org/10.3390/jmmp8030118

Academic Editors: Hamed Asgari and Elham Mirkoohi

Received: 26 April 2024
Revised: 22 May 2024
Accepted: 29 May 2024
Published: 31 May 2024

1. Introduction

Since the inception of sintered tungsten carbide cobalt (WC-Co) hardmetal by Karl Schröter in the 1920s, the pursuit among researchers and manufacturers to develop more efficient and cost-effective production methods for hardmetals with improved properties and intricate geometries has been ongoing. Also referred to as cemented carbides, hardmetals are composite materials comprising hard, brittle WC grains embedded within a soft, ductile metallic matrix, typically composed of Co, Fe, or Ni. Moreover, hardmetals often incorporate additional carbides like TiC, TaC, Cr_3C_2, NbC, or Mo_2C, which serve as inhibitors of WC-grain growth [1–3]. WC-10Co hardmetals are highly valued for their exceptional hardness and toughness, qualities that render them ideal for producing tools subjected to heavy impact and wear. These applications include the manufacturing of devices like anvils, cutters, slitters, and drills as well as tools used in cold-working and mining [4].

Additive manufacturing (AM) offers a compelling alternative for producing WC-Co components and is notable for its ability to create new geometries and cost-effectively produce small batches. Notably, AM allows the incorporation of complex features without increasing production costs, earning it its characterization as a "complexity for free" process [5]. Additive manufacturing technologies for hardmetals include beam-based methods

like directed energy deposition (DED), laser engineering net shaping (LENS) [6], direct laser fabrication (DLF) [7], selective laser sintering (SLS) [8,9], and selective laser melting (SLM) [10]. These methods sequentially produce each hardmetal layer, posing a challenge in managing anisotropy variations. In contrast, beamless methods like powder fused filament fabrication (PFFF), composite extrusion manufacturing (CEM), binder jetting (BJ), and 3D gel/direct-ink-write/robo-casting use a mix of powders and binder systems [11]. Indeed, in beamless methods, so-called "green parts" are constructed layer by layer. However, these parts require further post-treatment processes. This involves the removal of the binder or debinding and a sintering step, both of which are essential for achieving the final, fully structured part with the desired physical and mechanical properties [12]. Beamless methods tend to produce microstructures with lower residual stresses since the entire part is sintered simultaneously [11,13], overcoming the new layer cooling dynamics of beam-based AM methods [14].

The material extrusion process, particularly for polymeric filaments, was first patented by Stratasys [15] under the trademark of Fused Deposition Modelling or (FDM™). Later, the term fused filament fabrication (FFF) was introduced as an open, non-registered name for the technology [16]. Influenced by powder injection molding (PIM), PFFF was adapted to shape metals, ceramics, and composites in a three-step process: Shaping (by PIM or PFFF), debinding (solvent and/or thermal), and sintering (SDS) [17,18]. Pioneering research by Agarwala, et al. [19] led to the development of the first binder system for FFF processing of Si_3N_4 parts. Subsequent studies emphasized the need for tailored binder systems for different powdered materials [20].

In PFFF, the filament serves dual purposes as the extrusion driver and the extruded material. If the viscosity of the filament is too high or its strength too low, the feedstock can become unprintable, often failing due to buckling [21]. Additionally, the filament must withstand spooling processes and when printed, the part must support the internal pressure generated during solvent and thermal debinding, which might cause defects such as cracking and blistering [22,23]. Styrene-ethylene/butylene-styrene (SEBS) thermoplastic elastomers have been effective in PFFF binder formulations due to their flexibility and solubility in the first debinding stage [24–27]. When working with submicrometric particles, adding paraffin wax to SEBS in the binder system can effectively modulate viscosity and facilitate debinding [28].

Polyolefins such as polypropylene and polyethylene are commonly used as backbone materials. Nevertheless, materials such as EVA and PLA have been reported [28]. McNulty et al. [29] developed binder systems for the PFFF of lead zirconate titanate (PZT) samples, utilizing polyolefins and hydrocarbon resin. Their research demonstrated the potential of adapting commercially available materials to create PFFF-compatible feedstocks. Various research efforts, including those by Cano et al. [30] for ZrO_2 and Momeni et al. [31] for Al, have focused on using grafted and non-grafted polyolefins as backbones in PFFF feedstocks. These studies revealed improvements in powder dispersion and rheological behavior, accompanied by a slight increase in the viscosity of the feedstocks. Lengauer et al. [32] successfully printed, debinded, and sintered WC-10Co and Ti(C,N)-Co/Ni-based cermets using TPE as a soluble polymer and PP functionalized with maleic anhydride. They highlighted the need for optimized printing strategies to achieve defect-free microstructures, which aligns with Agarwala et al. [33] who developed printing strategies to rectify defects in Si_3N_4 and 17-4ph stainless steel (SS) printed by powder PFFF.

Additionally, Agarwala et al. [34] developed unique binder systems for WC-Co, SiO_2, 17-4 PH SS, Si_3N_4, and Al_2O_3, noting that smaller particle sizes in the same binder system, due to their increased surface area, resulted in higher viscosity in the feedstocks. This observation highlighted the need for reformulations incorporating different surfactants in the binder system to address this challenge. Surfactants based on fatty acids with long carbon chains, such as stearic acid (SA) are effective for WC-Co in polymeric binders, as demonstrated in various studies [35,36]. The viscosity of the feedstock, the geometrical factors of the liquefier system, and the layer height have been modeled to establish their

relationship with the extrusion force of ABS and PLA [37,38], allowing for a description aligned with the final properties of the printed material.

This study addresses the challenge of developing binder formulations and printing parameters for WC-10Co hard metals using powder PFFF. It provides a comprehensive analysis of how different binder compositions and printing variables impact the printing force, mechanical properties, and defect formation. The insights gained from this research aim to enhance the quality and performance of 3D-printed hard metal components, with significant implications for industries such as tooling and mining.

2. Materials and Methods

2.1. Materials

This study employed hardmetal ready-to-press powders, consisting of 10 wt% cobalt (Co) and a balance of tungsten carbide (WC). These powders underwent agglomeration using a spray drying process with an addition of 1 wt% paraffin wax, supplied by ZCC (Zhuzhou, China,). The binder systems included a combination of both soluble and non-soluble polymers. The soluble components comprised thermoplastic elastomer TPE (Sungallon, Shenzhen, China), paraffin wax (PW) as a viscosity modulator (Panreac, Barcelona, España), and stearic acid (SA) as a surfactant (Sigma Aldrich, Darmstadt, Germany). Additionally, the system incorporated a mixture of polypropylene random-copolymer (PP) (Essentia, Cartagena, Colombia) and polypropylene grafted with maleic anhydride (PP-MA), which served as the backbone.

Four different formulations were prepared to investigate the impact of backbone content and composition on the feedstocks. Backbone composition was varied using ratios of PP-MA to PP at 3:2 and 2:3. Additionally, two distinct backbone contents in the binder system of 26 wt% and 31 wt% were used. To offset variations in backbone content, additional TPE was added. Throughout the experiment, both SA and PW were kept constant (See Table 1).

Table 1. Formulated binder systems (52%vol) to be mixed with 48%vol WC-Co powders.

Binder	PP-MA	PP	TPE	PW [1]	SA
	wt. %	wt. %	wt. %	wt. %	wt. %
M1	18.62	12.42	46.56	18.00	4.40
M2	15.60	10.40	51.60	18.00	4.40
M3	12.42	18.62	46.56	18.00	4.40
M4	10.40	15.60	51.60	18.00	4.40

[1] The PW content of the RTP powder is included in the binder calculation.

The feedstocks were prepared using a shear-based mixing apparatus. Initially, the polymers underwent a homogenization process for 10 min, followed by the gradual addition of powders into the molten mixture in three distinct stages. The mixture was then continuously mixed for 60 min at a temperature of 160 °C. After mixing, the feedstocks were cut into small pieces, each measuring less than 5 mm in every dimension. These fragments were used to produce filament, employing a single-screw extruder with a 1.75 mm diameter die and operating at 180 °C. To assess changes in the binder system resulting from powder addition, 50 g of each binder type was mixed. However, the powder-free samples underwent an identical homogenization duration of 60 min to ensure a standardized comparison. To distinguish between the samples, 'M' without the suffix and 'P' will denote the binder system alone, while 'M + P' will indicate that the binder system was mixed with the hardmetal powder.

2.2. Thermal Properties

The thermal properties of the feedstocks and the binder systems were analyzed using differential scanning calorimetry (DSC) (Mettler Toledo). The materials were incrementally

heated from room temperature to 250 °C at a rate of 10 °C/min under a nitrogen flow of 50 mL/min. The crystallinity degree of each virgin polymer, binder system, and feedstock was calculated using the following formula [39]:

$$X_c = \frac{\Delta H_m}{\Delta H_m^0 * w} \quad (1)$$

where ΔH_m represents the fusion enthalpy (derived from the integral of the endothermic peak on the DSC curve), ΔH_m^0 is the enthalpy of fully crystalized PP (207 J/g) [40], and w is the weight fraction of PP in the analyzed sample.

To evaluate the thermal stability of both the binder systems and the feedstocks, a thermogravimetric analysis (TGA) (Mettler Toledo) was conducted. The samples were heated up to 700 °C at a rate of 10 °C/min under a nitrogen flow of 50 mL/min. During this process, the samples' weight and the rate of weight loss were measured.

2.3. Printing Force Measurements

A custom-built Arduino-based device was employed to measure the extrusion force of each filament. Equipped with two 5 kg load cells, this device featured a mechanism to maintain the FFF extrusion system's alignment and isolate it from the pulling motor. The filaments were tested at extrusion speeds of 7.5 and 10 mm/s and at temperatures of 200, 210, and 220 °C with 20 cm of tested filament in each run. Each experimental setup was replicated three times, with the resulting data being collected at a frequency of 0.2 Hz for further analysis to calculate the average extrusion force. The nozzle had a diameter of 0.6 mm, and the extrusion system was configured to mimic the standard FFF machine used in the printing experiments. The systematic error in measuring the extrusion force was determined to be less than 0.2 N. Care was taken to use 1.75 mm filaments to avoid errors due to the higher transversal area of any filaments.

2.4. Printing

An Ender 3 V2 FFF printer, specifically modified to include a direct extrusion drive system (Microswiss) and equipped with a 0.6 mm M2 steel hardened nozzle (Microswiss), was used to shape cylindrical samples with a diameter of 17 mm and a height of 7 mm. Five samples were printed at three different printing temperatures for each feedstock: 200, 210, and 220 °C for 80 samples (60 printed at 10 mm/s and 20 additional printed at 7.5 mm/s). The layer thickness and nozzle diameter settings were maintained at 0.3 mm and 0.6 mm, respectively. A printing flow of 103% was used for all the samples. Additional printing parameters are listed in Table 2.

Table 2. Key printing parameters utilized.

Infill Pattern	Number of External Lines	Infill Overlap	Retraction	Bed Temperature	Cooling Fan
Lines	1	50%	No	95 °C	Off

2.5. Debinding and Sintering

Following printing, the samples were immersed in cyclohexane for 72 h to remove the soluble polymers. Subsequently, a vacuum furnace performed the thermal debinding and sintering in a single step. As the focus of this study does not extend to a macro-scale analysis of the sintering and debinding stages, a non-optimized thermal debinding cycle was utilized. This cycle featured a heating rate of 0.2 °C/min between 400 and 550 °C and followed by a sintering plateau of 60 min at 1500 °C to achieve final densification of the samples. The sintering process for the samples was conducted within graphite containers to prevent decarburization and using an argon atmosphere for protection.

2.6. Characterization

The density of both printed and sintered samples was determined using the Archimedes method [41], with 99.9% ethanol employed to enhance wetting of the sample surfaces. To identify various defects post-printing and correlate them with the feedstocks and printing conditions used, a cryogenic three-point bending test was conducted on one sample from each feedstock configuration. The test setup involved placing the samples on two rods, each of which were 10 mm in diameter spaced 14 mm apart at their centers. A third rod of the same diameter was advanced at a rate of 1 mm/min until the sample fractured. Before testing, the green samples were immersed in liquid nitrogen for 10 min to ensure uniform internal temperature. After sintering, the samples were sectioned, subjected to diamond polishing for a smooth finish, and then analyzed. Both light-optical microscopy (OM) (Zeiss Z1.m) and scanning electron microscopy (SEM) (Phenom XL) were used to examine the green and sintered samples closely. The digital image software ImageJ™ (version 1.54g) was utilized for analyzing SEM micrographs to measure grain size.

3. Results and Discussion

3.1. Thermal Properties

3.1.1. DSC Analysis

Figure 1 shows the DSC thermograms of the raw materials, binder systems and feedstocks. Unmodified polypropylene (PP) exhibits a notably lower melting point compared to polypropylene grafted with maleic anhydride (PP-MA). This difference is highlighted by two distinct fusion peaks in the PP curve, attributed to the melting of co-monomers added to enhance the polymer fluidity, with the second peak representing the complete melting of the polymeric chain including the propylene co-monomer. Interestingly, the thermoplastic elastomer (TPE) shows a minor endothermic reaction at 62 °C, which vanishes upon integration into the feedstocks. The DSC thermograms' data, including melting temperature T_m, fusion enthalpy ΔH_m, start and end temperatures of the melting reaction, and degree of crystallinity derived from Equation (1), are quantitatively summarized in Table 3. While the feedstocks and binder systems displayed negligible variations in melting points, a pronounced influence of fusion enthalpy was observed relative to backbone content and the presence of PP-MA. This indicates that a mere 5% substitution of the backbone with TPE fosters a significant interaction between the PP and TPE chains, diminishing their crystallization capability and impacting their fusion enthalpy.

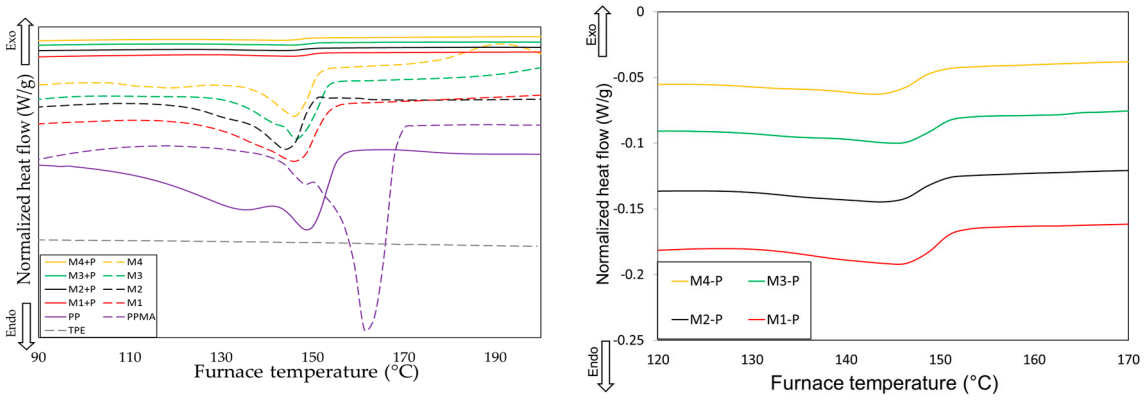

(**a**) (**b**)

Figure 1. DSC curves of the following: (**a**) raw polymers, binder systems and binder systems mixed with WC-10Co powders; (**b**) magnification of binder systems mixed with the powders.

Table 3. Calculated data.

Description	T_m [C°]	T Onset [C°]	T Endset [C°]	ΔH_m $\left[\frac{J}{g}\right]$	X_c [%]
PP	148.59	133.5	155.7	91.03	43.98%
PP-MA	161.05	153.7	168.5	105.18	50.81%
TPE	-	-	-	-	-
M1	145.93	123.76	153.54	41.19	54.32%
M1 + P	145.63	128.18	151.51	1.72	43.20%
M2	144.22	130.40	149.86	29.33	46.24%
M2 + P	144.43	123.42	150.32	1.04	31.20%
M3	145.76	135.56	153.74	32.46	45.25%
M3 + P	145.69	125.76	151.48	0.88	22.07%
M4	146.06	133.25	151.68	18.23	28.76%
M4 + P	143.59	126.31	149.55	0.83	24.77%

The crystallinity of the feedstocks exhibited a pronounced dependency on the PP-MA content. Notably, the M1 sample, with the highest PP-MA concentration, exhibited increased crystallinity upon integration with powders. This contrasts with the behavior observed in the other mixtures (M2, M3, and M4), where despite varying levels of PP-MA content, there was an overall decrease in crystallinity following the addition of WC-10Co powder. The enhancement in crystallinity within a polymeric matrix due to powder addition is attributed to the creation of multiple nucleation sites [39]. The lack of increased crystallinity in mixtures M2, M3, and M4 underscores the critical role of surface interactions between the powder and the polymer matrix in the nucleation process, which is significantly influenced by the non-polar characteristics of PP. The onset and endset temperatures of the melting process are affected by the amount of PP-MA in the mixture, suggesting an interaction between the polar properties of PP-MA and the powder surfaces.

3.1.2. TGA Analysis

The degradation profiles of the raw materials, as shown in the TGA analysis presented in Figure 2a, reveal distinct rates and temperatures of thermal decomposition. PP-MA exhibits an onset of degradation at lower temperatures compared to PP, likely attributable to the incorporation of maleic anhydride. Notably, the thermal decomposition residuals at 700 °C for PP and PP-MA are 0.029% and 0.190%, respectively. This disparity suggests that feedstocks with a higher proportion of PP-MA could have a pronounced impact on the carbon content in the final printed samples due to incomplete combustion. Moreover, the M1-P sample, enriched with PP-MA, demonstrates a higher thermal degradation onset than other feedstocks. This observation may indicate a stronger interaction between the polar maleic anhydride component and the surfaces of the powders, as the proportion of the grafted backbone increases. Such interactions indicate enhanced thermal stability, which could benefit the performance of printed materials under elevated temperatures.

The backbone content and the proportion of PP-MA within it had a noticeable impact on the derivative mass change, as seen in Figure 2b. It was observed that samples with a higher backbone content exhibited more significant rates of mass change. This, in turn, lead to increased internal pressures within the part during the thermal debinding process. Furthermore, within the groups containing 31% (M1 and M3) and 26% (M2 and M4) backbone content, the degradation temperature varied depending on the presence of PP-MA. This variation suggests that the PP-MA component within the backbone may significantly influence the material's thermal stability and degradation behavior during processing. The feedstocks M2-P and M4-P exhibited a slight mass loss of 0.25% before reaching 200 °C, likely due to the volatilization of the low molecular weight additives contained within the used high fluidity PP, which are more predominant in these samples.

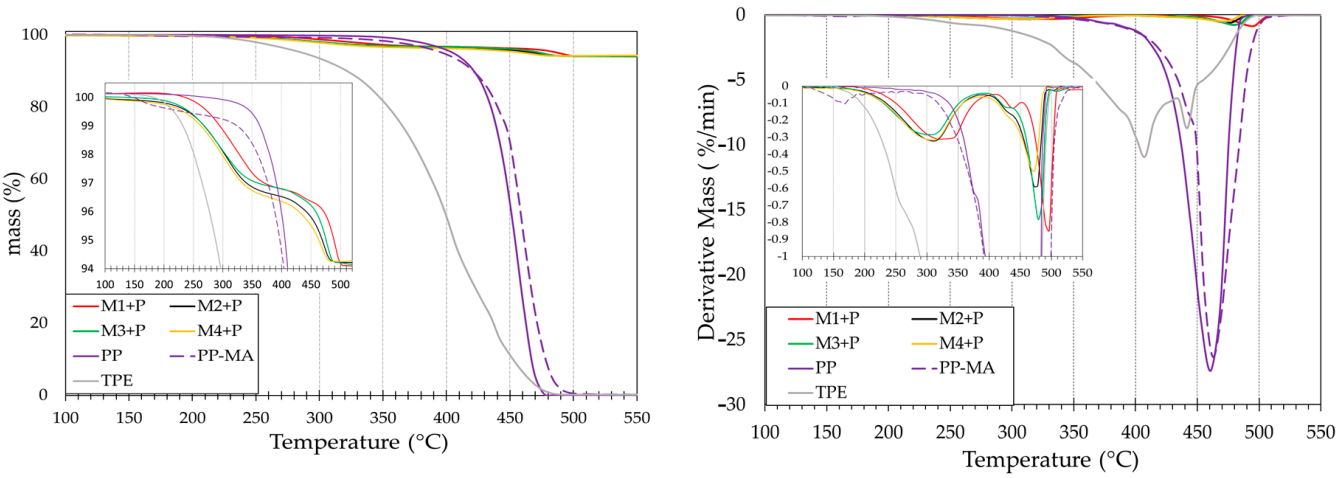

Figure 2. TGA results of the studied feedstocks: (**a**) mass-loss temperature diagram; (**b**) derivative mass calculation.

3.2. Force Measurement Analysis

Various researchers have explored the rheology of powder mixtures with polyolefins and TPE [42]. Given the non-Newtonian behavior of these types of raw materials, it is understood that with an increase in shear rate, there is a reduction in viscosity [35]. However, in the practical context of PFFF printing, the extrusion force as a response variable has been related to the sum of pressure drops in three areas: the start of the nozzle, the section change zone, and the capillary or nozzle exit zone; this dependency is influenced by geometric factors, rheological properties of the material, and mass flow [37,43]. Since these three zones were replicated identically to those in the printer within our force measurement device, the powder loading is constant, and the testing conditions are the same. Any increase or decrease in the measured printing force accurately reflects the material response of the manufactured filaments. In agreement with other authors, Figure 3 clearly shows that increasing the extrusion temperature is often suggested to reduce high filament viscosities, as this process lowers the printing force by boosting the mobility of the polymer chains.

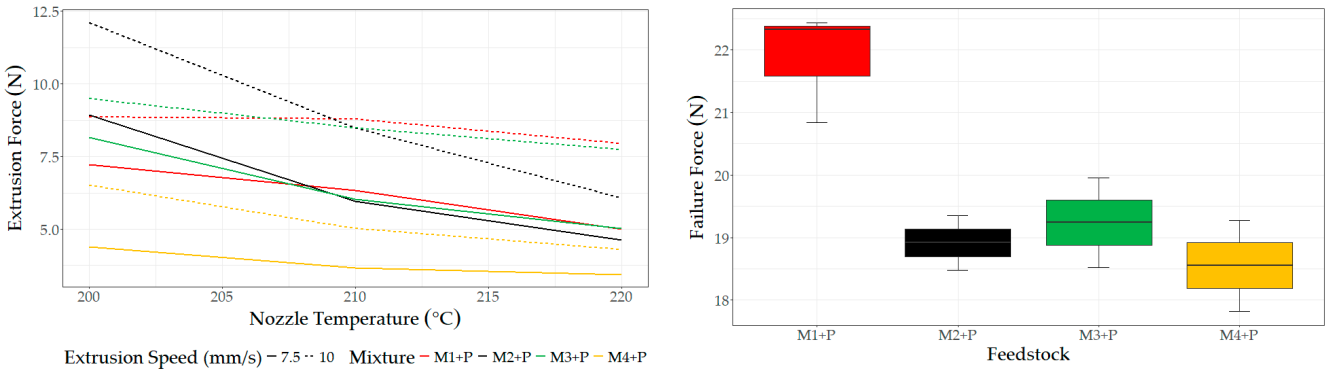

Figure 3. Force measurements for manufactured feedstocks: (**a**) variation with temperature and extrusion speed; (**b**) test at ambient temperature leading to filament failure.

The mean extrusion force for the four different feedstocks as a function of extrusion speed and nozzle temperature is illustrated in Figure 3a. The analysis demonstrates that extrusion speed significantly impacts the extrusion force across all tested conditions. Despite the anticipated increase in shear rate with higher extrusion speeds, the 7.5 mm/s

speed resulted in a lower extrusion force for all feedstocks and temperatures tested. Notably, the M4-P feedstock displayed the lowest extrusion force, suggesting it had the lowest viscosity among all samples. This finding is consistent with literature on non-grafted PP, which posits that the absence of grafting agents, such as maleic anhydride, might lead to decreased material viscosity, easing the extrusion process [44].

Conversely, the M1-P feedstock maintained an extrusion force below that of the 10 mm/s speed and nearly identical to the 7.5 mm/s conditions compared to the M2 and M3 samples. This variance may be attributed to enhanced powder dispersion facilitated by the higher PP-MA content, resulting in improved distribution within the polymer matrix. The M2-P and M3-P feedstocks exhibited higher extrusion forces at lower temperatures, with notable variability as the printing temperature increased. In contrast, the M1-P feedstock demonstrated the highest printing force at 220 °C. This behavior could be explained by the robust particle-polymer interactions of PP-MA, as indicated by the TGA analysis.

The maximum force or failure force of the developed filaments is reported in Figure 3b. It can be observed that the M1-P sample exhibited significantly greater resistance than the other samples, which did not show significant differences compared to each other. This outcome directly results from two factors: a better adhesion between the powders and the polymer matrix, attributed to the higher PP-MA content, and a higher achieved crystallinity of the feedstock. Additionally, the higher load capacity also implies a lower probability of process failure, thereby enhancing reliability. However, the M2, M3, and M4 feedstocks demonstrated a load capacity that required only a maximum of 50% of their failure force under the shown printing conditions. Their reduced capacity can be attributed to a higher content of TPE in the cases of M2 and M4 mixtures and to a lower ratio of PP-MA/PP for the M2 sample. All filaments failed due to lateral abrasion caused by the pushing rollers of the FFF system. For productivity reasons and because the speed of 10 mm/s was significantly below the load capacity, this value was chosen for conducting the first run of printing experiments.

3.3. Samples Printed at 10 mm/s and Different Temperatures

Following the measurement of green densities and the calculation of relative green densities, assumptions were tested, and a two-way ANOVA was conducted, revealing significant effects from both the printing temperature and feedstock as well as an interaction between the printing temperature and the feedstock, as shown in Table 4. The findings depicted in Figure 4 align with the ANOVA results, demonstrating varied behavior in the relative green density across different feedstocks and printing temperatures. Samples closest to the median density were chosen for cryogenic three-point bending tests to analyze the internal defects of the samples. Figure 5 demonstrates the samples printed at 200 and 220 °C post cryogenic three-point bending, with 210 °C printed samples in the Supplementary Material. Defects are highlighted through SEM-BSE magnification.

Table 4. Results of the two-way ANOVA for green density of printed samples.

Source of Variation	Degrees of Freedom	Sum Sq	Mean Sq	*p* Value
Temperature	2	5.88	8.78	5.65×10^{-4}
Feedstock	3	8.38	8.33	1.46×10^{-4}
Temperature: Feedstock	6	15.18	7.55	9.89×10^{-6}
Residuals	48	16.09		

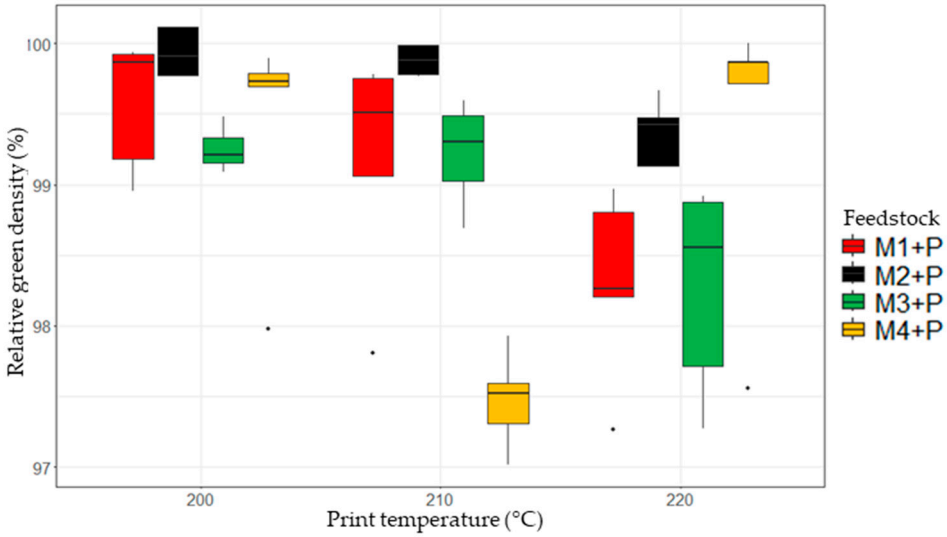

Figure 4. Relative green densities for different feedstocks and printing temperatures.

The PP/PP-MA ratio significantly influences relative density and its temperature-dependent variability. The relative green densities of the printed samples, presented in Figure 4, show that while M4-P samples faced significant green density fluctuations due to their high PP/PP-MA and TPE content, M2-P, with a lower PP/PP-MA ratio, showed better performance and stability. This difference is attributed to the M2-P feedstock's improved powder and polymer matrix compatibility, minimizing issues like material dragging and nozzle sticking, hence ensuring more accurate material deposition and print line solidification. The variability in the M4-P feedstock is a result of reduced interactions between the powder surfaces and the polymer matrix, causing material dragging, inaccurate placement, solidification of print lines, and a material's propensity to stick in the nozzle, leading to material accumulation on the sides of the printed samples.

The cryogenic fracture enabled the identification of various defects within the printed samples; some were influenced by the printing temperature, while others stemmed from the specific feedstock used. At 220 °C, all samples exhibited excess material, particularly noticeable in samples with high TPE content (M2-P and M4-P), which led to accumulation in the lower side areas of the samples as shown in Figure 5a–d. In contrast, at 200 °C, two main types of defects were more frequently observed: the "mountain-type" defect, resulting from material overflow from one print layer to another and creating areas of excess material that could interfere with the accurate placement or thorough filling of subsequent layers as well as gaps in and between infill lines due to a lack of material to be extruded. These defects, illustrated in Figure 5e–h, may be exacerbated by filament diameter variability. However, the capacity of each feedstock to minimize "mountain-type" defects or gaps between infill lines indicates a feedstock-specific response that ultimately influences the green density of the printed samples. Therefore, green density metrics could reliably reflect a feedstock's effectiveness in producing high-quality printed components.

In Figure 4, it is evident that an increase in temperature had a reducing effect on the relative green density of the samples. Furthermore, TGA analysis indicates slight mass loss before 220 °C, likely from moisture desorption or low molecular weight polymer chain degradation, leading to gas generation during printing [45]. This may result in gas entrapment within print lines, affecting green density as depicted in Figure 5a–d. These results agree with studies on polymeric materials, suggesting that utilizing higher printing temperatures to reduce high viscosities is highly dependent on the thermal stability and dryness of the feedstock [46].

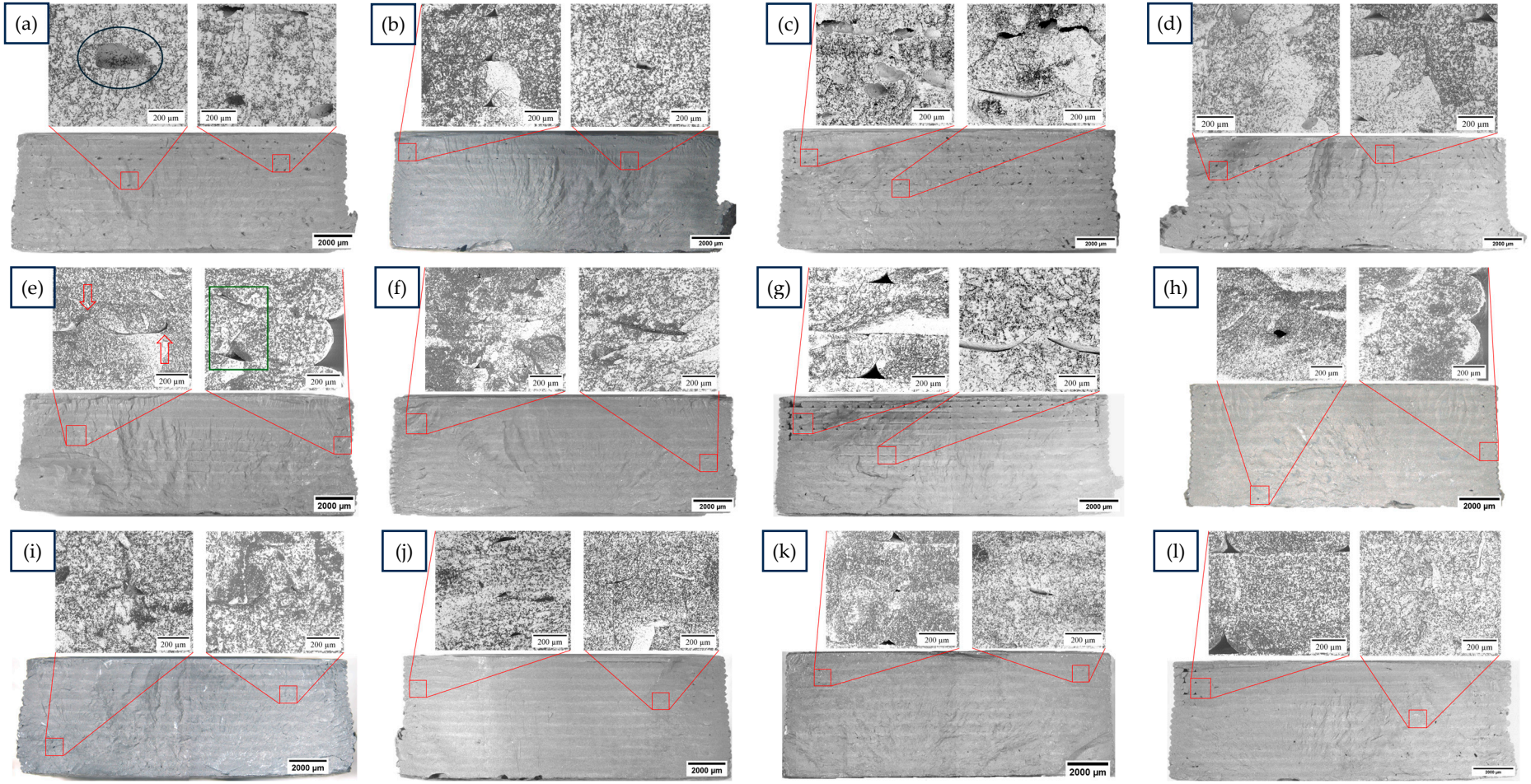

Figure 5. SEM-BSE details of some defects and optical microscopy of the green samples after cryogenic fracture of different feedstocks: (**a**–**d**) M1-P, M2-P, M3-P, M4-P respectively, at 220 °C and 10 mm/s; (**e**–**h**) M1-P, M2-P, M3-P, M4-P respectively, printed at 200 °C and 10 mm/s; (**i**–**l**) M1-P, M2-P, M3-P, M4-P respectively, printed at 200 °C and 7.5 mm/s.

3.4. Samples Printed at 7.5 mm/s

Despite some defects, the superior green density outcomes for all the samples printed at 200 °C inspired a hypothesis about the impact of printing speed. The findings depicted in Figure 3a showed that a slower speed of 7.5 mm/s significantly reduced the printing force, implying a quicker attainment of this force level and a shorter delay in material output. Additionally, a reduced printing speed may allow more time for the material to fill the voids identified in samples printed at a faster speed of 10 mm/s. After printing, the cryogenic fracture of the samples was conducted, as shown in Figure 5i–l. The size and quantity of defects were reduced, indicating a positive effect of the printing speed. However, a two-way ANOVA test indicated no significant impact of printing speed on green density outcomes for samples printed at 200 °C (see Table 5) due to data dispersion and the challenge of achieving densities near the theoretical 100%, as observed in Figure 6a. Notably, a significant interaction between speed and feedstock was observed, particularly with M4-P samples, which encountered more pronounced adhesion issues at lower speeds, highlighting increased material adhesion in the nozzle and worsening material dragging.

Table 5. Results of the two-way ANOVA for green density of printed samples at different feedstocks and velocity.

Source of Variation	Degrees of Freedom	Sum Sq	Mean Sq	*p* Value
Velocity	1	0.156	0.1563	0.32372
Feedstock	3	2.183	0.7277	0.00806
Velocity: Feedstock	3	1.372	0.4572	0.04800
Residuals	32	4.978	0.1556	

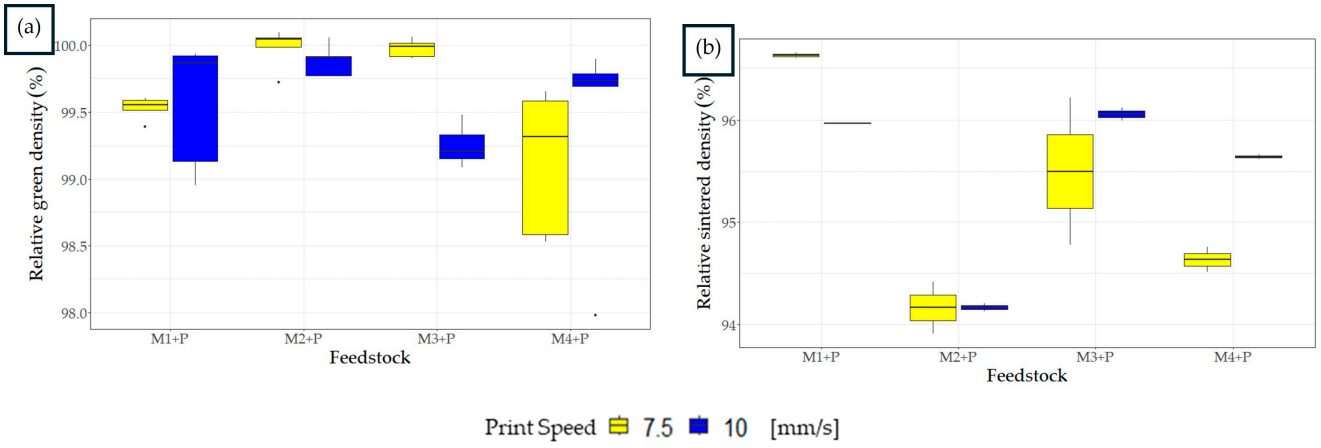

Figure 6. Relative densities of the samples printed at 200 °C at different speeds: (**a**) green state, (**b**) after sintering.

3.5. Sintered Samples

No clear relationship was found between the green and sintered relative densities, indicating possible internal defect formation (see Figure 7a,b) during solvent and thermal debinding processes. The relative sintered density illustrated in Figure 6b highlights significant differences in densities and variances Although the M1-P sample did not have the highest green density, its higher PP-MA content led to improved sintered density. Conversely, the M2-P feedstock with high green density showed significant variation in sintered density. One reason for the crack formation and further reduction in density during debinding could be attributed to internal pressures during thermal debinding [47,48]. Nevertheless, due to the very low heating speed used in the thermal debinding process, it is difficult for built-up pressures to damage the part [25]. Several studies have related the swelling of the binders during the solvent debinding process as a source of internal

defects such as cracks and slumping [22,23,28]. These defects could be enhanced by the low diffusivity of the solvent in the sample due to small particle size [49]. This may explain the blisters observed in the first layers in Figure 7b as a stress-related defect caused by the gradient in solvent diffusion within the sample. Better adhesion between printing lines, as seen in the M1-P feedstock, can mitigate this phenomenon, as shown in Figure 7a. A detailed study focused on internal defects after solvent debinding is required to confirm this phenomenon.

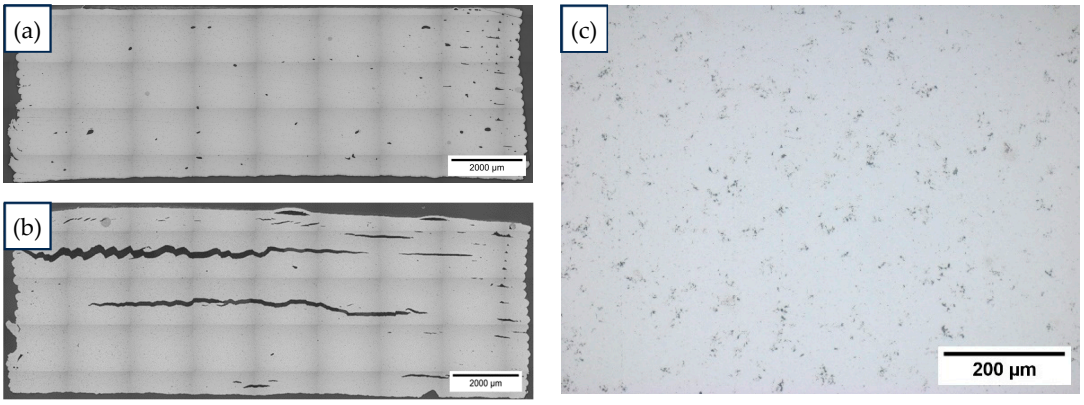

Figure 7. Metallographic images of representative results of the sintered samples: (**a**) printed with the M1-P feedstock at 200 °C and 10 mm/s, (**b**) printed with the M2-P feedstock at 200 °C and 10 mm/s, (**c**) 200× micrograph showing carbon precipitation and micropores found in all the samples. The 200× micrographs of the other samples printed at 200 °C can be found in the Supplementary Material.

Optical microscopy of the polished samples reveals carbon precipitation mixed with some porosity clearly visible at 200×. According to ASTM B276-21 [50], the observed porosities for the M1 + P samples are classified as A02-B00-C06, while the remaining samples are classified as A02-B00-C04. This apparent increase in the residual carbon in the M1 + P feedstock (Figure 7c) can be attributed to the higher residual carbon found in the TGA for the PP-MA. The SEM micrographs of the sintered samples printed at 200 °C are depicted in Figure 8. All microstructures exhibit zones of carbon precipitation in the Co matrix, likely resulting from excess carbon originating from the degradation of the polymeric chains in the backbone, which reduces the measured density of the sintered samples. To address this issue, a reductive atmosphere in thermal debinding will be required to remove this excess carbon [32].

The WC particles in the sintered samples showcase typical faceted structures characteristic of liquid phase sintering [51] along with abnormal grain growth due to the absence of grain growth inhibitors. This observation underscores the necessity of optimizing the sintering cycle for components fabricated through PFFF to enhance their microstructural properties [52]. The absence of noticeable Co segregation or WC distribution issues in the microstructure suggests that adjusting the polymeric raw materials for feedstock improvement is feasible without negatively impacting the microstructural integrity. This opens possibilities for refining the feedstock formulation to enhance the printing process and the final properties of the printed parts.

The amount of raw polymeric materials varied for each formulated feedstock, yet the microstructures displayed only minor variations in WC grain size and distribution, with mean values between 1.42 and 1.48 µm (refer to Figure 9a) indicating a limited influence of the formulated binder systems. Only the M2-P feedstock tended to develop more considerable abnormal grain growth. This suggests that the hardness variability noted in Figure 9b could be attributed to subsurface macro defects.

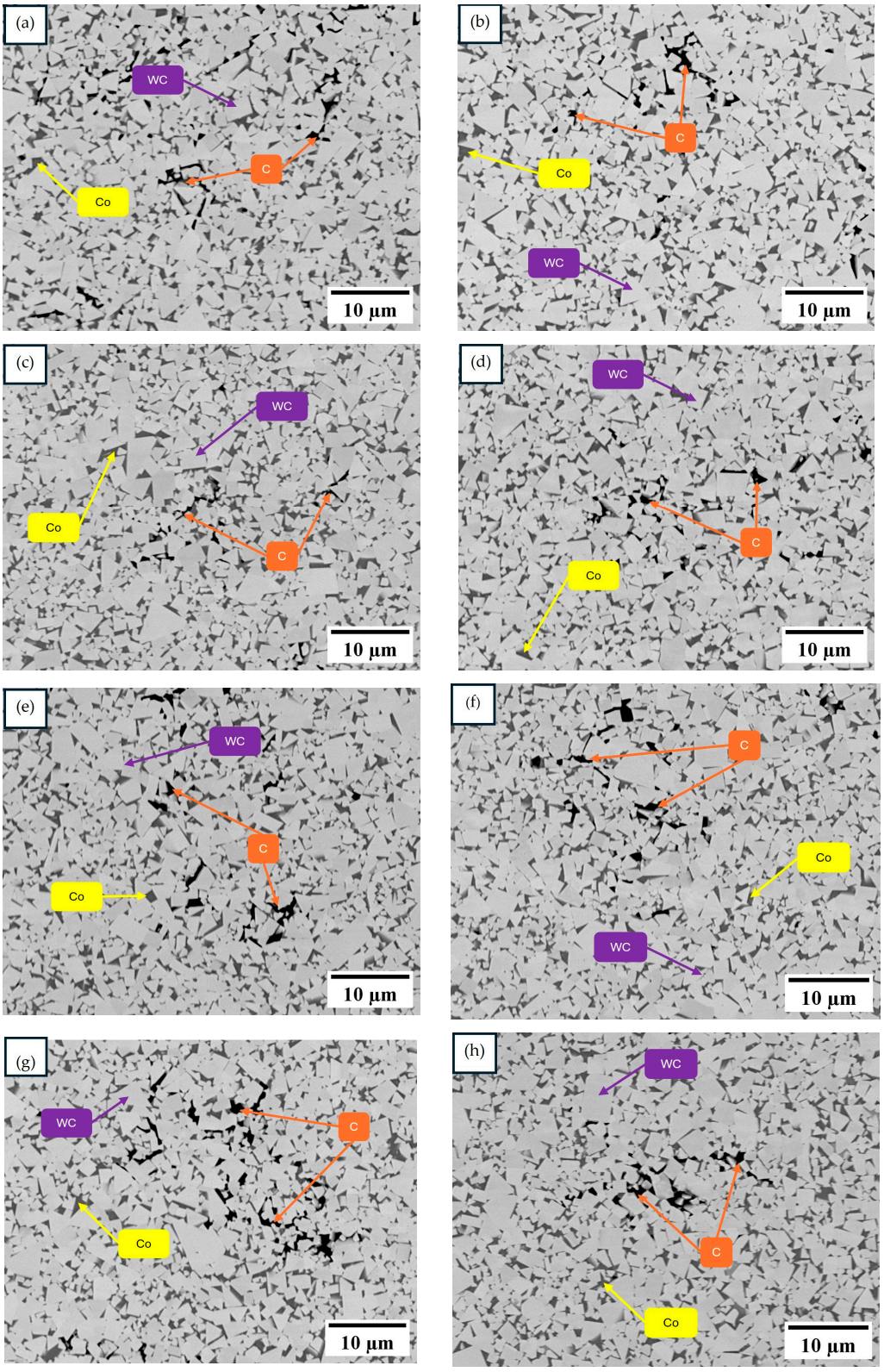

Figure 8. Backscattered SEM micrographs of the sintered samples printed at 200 °C made with the developed feedstocks and centered in the carbon precipitated areas printed at different speeds: (**a**) M1-P at 10 mm/s, (**b**) M1-P at 7.5 mm/s, (**c**) M2-P at 10 mm/s, (**d**) M2-P at 7.5 mm/s, (**e**) M3-P at 10 mm/s, (**f**) M3-P at 7.5 mm/s, (**g**) M4-P at 10 mm/s, and (**h**) M4-P at 7.5 mm/s.

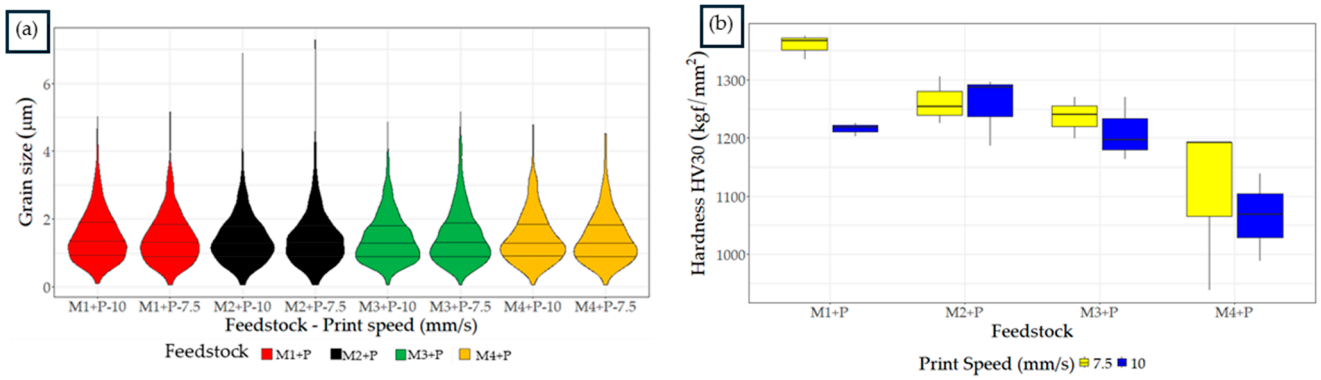

Figure 9. Developed feedstocks after printing at 200 °C and sintering at 1500 °C: (**a**) Violin plot of grain size from data obtained with digital image processing; (**b**) Vickers hardness.

A two-way ANOVA (Table 6) on hardness response highlighted the significant impact of printing speed, unlike green density, underscoring the critical balance between layer adhesion and defect avoidance for successful debinding and sintering of the parts. Printing defects observed in Figure 10a–c are examples of how defects formed during the printing stage persist post-sintering, with a notable rounding effect primarily due to the capillary forces of liquid cobalt. This phenomenon causes defects with a low form factor, like those shown in Figure 10a, to increase in height, negatively impacting the density of the sintered material and, consequently, its mechanical properties. This phenomenon suggests that cracks or defects formed during the solvent or thermal debinding process could worsen during sintering due to capillary force deformation.

Table 6. Results of the two-way ANOVA for sintered density of the samples printed at 200 °C.

Source of Variation	Degrees of Freedom	Sum Sq	Mean Sq	*p* Value
Velocity	1	17,672	3.782	0.0696
Feedstock	3	47,619	10.192	0.0005
Velocity: Feedstock	3	5685	1.217	0.3358
Residuals	16	4672		

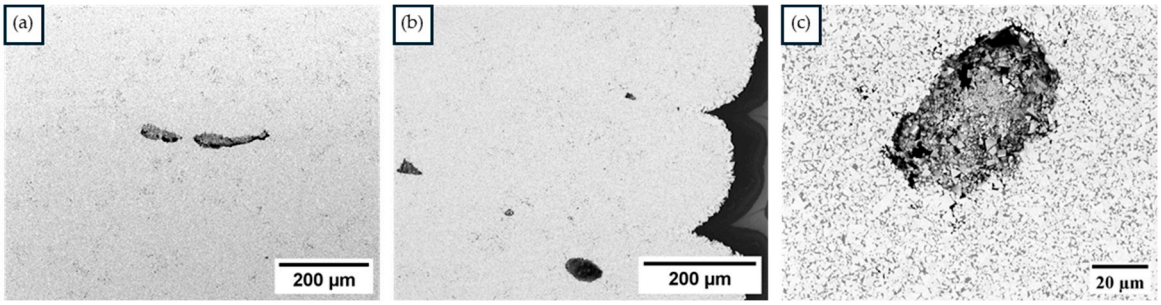

Figure 10. Persistence of printing defects after the sintering process: (**a**) mountain-like defect found in M2-P feedstock; (**b**) lack of filling between internal infill lines and the outer layer found in M4-P Feedstock; (**c**) entrapped gas found in M3-P feedstock.

The findings from this study pave the way for future research focused on optimizing WC-10Co feedstocks and conducting comprehensive analyses of solvent and thermal debinding processes.

4. Future Perspectives and Limitations

The application of PFFF for fabricating WC-10Co hardmetal parts presents both promising opportunities and notable challenges. Future research should focus on optimizing binder formulations to enhance mechanical properties and reduce defects during thermal and solvent debinding processes and address design metrics. Limitations, such as the need for precise control over printing parameters and the susceptibility to internal defects due to diffusion-related and thermal stresses, must be addressed. This technique shows potential as an alternative for small-batch manufacturing of medium-sized and small hardmetal tools, such as cutting tools and mold inserts.

5. Conclusions

Four distinct feedstocks were developed and assessed for their performance in PFFF of WC-10Co samples, providing a foundation for future studies to refine depolymerization and sintering pathways, while establishing a foundational understanding of the importance of feedstock and processing variables. The main findings of this study include the following:

- Feedstocks with lower printing forces tended to develop more defects, which persisted through the liquid phase sintering process.
- Enhancing the ratio of PP-MA to PP within the feedstock improved particle-binder interactions, reducing material dragging and defects during the debinding and printing processes.
- Adjusting printing speeds proved to be a more effective method for reducing printing forces compared to increasing printing temperatures. This adjustment significantly impacts the mechanical properties of printed parts.
- This study provides insights into the importance of binder system compatibility with the powder surface, influencing the sintering process outcomes.

Supplementary Materials: The following supporting information can be downloaded at: https://www.mdpi.com/article/10.3390/jmmp8030118/s1, Figure S1. SEM-BSE details and Optical Microscopy of the Green Samples printed at 10 mm/s after cryogenic fracture for the different feedstocks printed at 210 °C; Figure S2. Optical Microscopy of the samples printed at 200 °C after sintering, printed at different speeds.

Author Contributions: Conceptualization, J.D.R.B.; methodology, J.D.R.B.; software, J.D.R.B.; validation, J.D.R.B., A.F.G.P., L.K.H.Q. and L.A.B.M.; formal analysis, J.D.R.B.; investigation, J.D.R.B., A.F.G.P.; resources, A.F.G.P., L.K.H.Q. and L.A.B.M.; data curation, J.D.R.B.; writing—original draft preparation, J.D.R.B.; writing—review and editing, J.D.R.B., A.F.G.P., L.K.H.Q. and L.A.B.M.; visualization, J.D.R.B.; supervision, L.K.H.Q. and L.A.B.M.; project administration, L.K.H.Q.; funding acquisition, L.K.H.Q. All authors have read and agreed to the published version of the manuscript.

Funding: The authors thank the Powder Metallurgy Laboratory of "Universidad Nacional de Colombia Sede Bogota" and the "Centro de Materiales y Ensayos of SENA, Regional Distrito Capital SGPS-12351-2024" for the logistical, technical, human, and financial support of the project. The project funded this research, "Technological development for the manufacture of metal tools using additive manufacturing techniques based on extrusion for high temperature and wear applications used by the Colombian auto parts industry" with the code 82305—110189082305 and contingent recovery financing contract number 2021–1012 of 2021 celebrated between the Colombian institute of educational credit and technical studies abroad, "Mariano Ospina Pérez"—ICETEX, the Ministry of Science, Technology and Innovation, and the National University of Colombia.

Data Availability Statement: The data presented in this study are available on request from the corresponding author due to restrictions associated with the policies of the projects that funded the research.

Conflicts of Interest: The authors declare no conflicts of interest.

References

1. Mahmoodan, M.; Aliakbarzadeh, H.; Gholamipour, R. Sintering of WC-10%Co Nano Powders Containing TaC and VC Grain Growth Inhibitors. *Trans. Nonferrous Met. Soc. China* **2011**, *21*, 1080–1084. [CrossRef]
2. Farag, S.; Konyashin, I.; Ries, B. The Influence of Grain Growth Inhibitors on the Microstructure and Properties of Submicron, Ultrafine and Nano-Structured Hardmetals—A Review. *Int. J. Refract. Met. Hard Mater.* **2018**, *77*, 12–30. [CrossRef]
3. Rubiano Buitrago, J.D.; Gil Plazas, A.F.; Herrera Quintero, L.K. Influence of TiC and Cr_3C_2 Additions on the Mechanical Properties of a (W-Ti-Cr)C-Co Sintered Hardmetal. *J. Mater. Res. Technol.* **2019**, *8*, 5736–5744. [CrossRef]
4. Upadhyaya, G.S. Classification and Applications of Cemented Carbides. In *Cemented Tungsten Carbides*; William Andrew Publishing: Westwood, NJ, USA, 1998; pp. 288–308, ISBN 978-0-8155-1417-6.
5. Quinlan, H.E.; Hasan, T.; Jaddou, J.; Hart, A.J. Industrial and Consumer Uses of Additive Manufacturing: A Discussion of Capabilities, Trajectories, and Challenges. *J. Ind. Ecol.* **2017**, *21*, S15–S20. [CrossRef]
6. Xiong, Y.; Smugeresky, J.E.; Schoenung, J.M. The Influence of Working Distance on Laser Deposited WC-Co. *J. Mater. Process. Technol.* **2009**, *209*, 4935–4941. [CrossRef]
7. Li, Y.; Bai, P.; Wang, Y.; Hu, J.; Guo, Z. Effect of Ni Contents on the Microstructure and Mechanical Properties of TiC-Ni Cermets Obtained by Direct Laser Fabrication. *Int. J. Refract. Met. Hard Mater.* **2009**, *27*, 552–555. [CrossRef]
8. Zong, G.; Wu, Y.; Tran, N.; Lee, I.; Bourell, D.L.; Beaman, J.J.; Marcus, H.L. Direct Selective Laser Sintering of High Temperature Materials. *Proc. Solid Free. Fabr. Symp.* **1992**, 72–85.
9. Kumar, S.; Czekanski, A. Optimization of Parameters for SLS of WC-Co. *Rapid Prototyp. J.* **2017**, *23*, 1202–1211. [CrossRef]
10. Uhlmann, E.; Bergmann, A.; Bolz, R.; Gridin, W. Application of Additive Manufactured Tungsten Carbide Tool Electrodes in EDM. *Procedia CIRP* **2018**, *68*, 86–90. [CrossRef]
11. Vaezi, M.; Drescher, P.; Seitz, H. Beamless Metal Additive Manufacturing. *Materials* **2020**, *13*, 922. [CrossRef]
12. Gonzalez-Gutierrez, J.; Cano, S.; Schuschnigg, S.; Kukla, C.; Sapkota, J.; Holzer, C. Additive Manufacturing of Metallic and Ceramic Components by the Material Extrusion of Highly-Filled Polymers: A Review and Future Perspectives. *Materials* **2018**, *11*, 840. [CrossRef] [PubMed]
13. Aramian, A.; Razavi, S.M.J.; Sadeghian, Z.; Berto, F. A Review of Additive Manufacturing of Cermets. *Addit. Manuf.* **2020**, *33*, 101130. [CrossRef]
14. Leary, M. Chapter 12 - Directed Energy deposition. In *Additive Manufacturing Materials and Technologies*; Elsevier: Amsterdam, The Netherlands, 2020; pp. 321–334. [CrossRef]
15. Scott, S. Apparatus and Method for Creating Three-Dimensional Objects. *Bunseki Kagaku* **1992**, *28*, 195–196. [CrossRef]
16. Sells, E.; Bailard, S.; Smith, Z.; Bowyer, A.; Olliver, V. RepRap: The Replicating Rapid Prototyper: Maximizing Customizability by Breeding the Means of Production. *Handb. Res. Mass Cust. Pers.* **2009**, 568–580. [CrossRef]
17. Kukla, C.; Gonzalez-Gutierrez, J.; Cano Cano, S.; Hampel, S.; Burkhardt, C.; Moritz, T.; Holzer, C. Fused Filament Fabrication (FFF) of PIM Feedstocks. In *Actas del VI Congreso Nacional de Pulvimetalurgia y I Congreso Iberoamericano de Pulvimetalurgia*; Herranz, G., Ferrari, B., Cabrera, J.M., Eds.; Comité Español de Pulvimetalurgia: Ciudad Real, Spain, 2017; Volume 6, pp. 1–6.
18. Suwanpreecha, C. A Review on Material Extrusion Additive Manufacturing of Metal and How It Compares with Metal Injection Moulding. *Metals* **2022**, *12*, 429. [CrossRef]
19. Agarwala, M.K.; Bandyopadhyay, A.; Van Weeren, R. Fused Deposition of Ceramics (FDC) for Structural Silicon Nitride Components. *Int. Solid Free. Fabr. Symp.* **1996**, 336–344. [CrossRef]
20. Agarwala, M.K.; van Weeren, R.; Bandyopadhyay, A.; Safari, A.; Danforth, S.C.; Priedeman, W.R. Filament Feed Materials for Fused Deposition Processing of Ceramics and Metals. In *Proceedings of the Solid Freeform Fabrication Symposium*; The University of Texas at Austin: Austin, TX, USA, 1996; pp. 451–458.
21. Venkataraman, N.; Rangarajan, S.; Matthewson, M.J.; Harper, B.; Safari, A.; Danforth, S.C.; Wu, G.; Langrana, N.; Guceri, S.; Yardimci, A. Feedstock Material Property—Process Relationships in Fused Deposition of Ceramics (FDC). *Rapid Prototyp. J.* **2000**, *6*, 244–252. [CrossRef]
22. Hwang, K.S.; Lin, H.K.; Lee, S.C. Thermal, Solvent, and Vacuum Debinding Mechanisms of PIM Compacts. *Mater. Manuf. Process.* **1997**, *12*, 593–608. [CrossRef]
23. Kukla, C.; Cano, S.; Kaylani, D.; Schuschnigg, S.; Holzer, C.; Gonzalez-Gutierrez, J. Debinding Behaviour of Feedstock for Material Extrusion Additive Manufacturing of Zirconia. *Powder Metall.* **2019**, *62*, 196–204. [CrossRef]
24. Elkins, K.; Nordby, H.; Janak, C.; Gray, R.W.; Bohn, J.H.; Baird, D.G. Soft Elastomers for Fused Deposition Modeling. In Proceedings of the Eighth Solid Freeform Fabrication (SFF) Symposium, Austin, TX, USA, 11–13 August 1997; pp. 441–448.
25. Gil-Plazas, A.-F.; Rubiano-Buitrago, J.-D.; Boyacá-Mendivelso, L.-A.; Herrera-Quintero, L.-K. Solid-State and Super Solidus Liquid Phase Sintering of 4340 Steel SLM Powders Shaped by Fused Filament Fabrication. *Rev. Fac. Ing.* **2022**, *31*, e13913. [CrossRef]
26. Godec, D.; Cano, S.; Holzer, C.; Gonzalez-Gutierrez, J. Optimization of the 3D Printing Parameters for Tensile Properties of Specimens Produced by Fused Filament Fabrication of 17-4PH Stainless Steel. *Materials* **2020**, *13*, 774. [CrossRef]
27. Coelho, S.; Magro, A.; Texeira, P.; Ferreira, N.; Pereira, P.; Rodrigues, F.; Jorge, H.; Sacramento, J. Development of Formulations of WC-Co Filament for Fused Filament Fabrication. In Proceedings of the EURO PM 2020: European Conference on Powder Metallurgy, online, 5–7 October 2020.

28. Cano, S.; Gonzalez-Gutierrez, J.; Sapkota, J.; Spoerk, M.; Arbeiter, F.; Schuschnigg, S.; Holzer, C.; Kukla, C. Additive Manufacturing of Zirconia Parts by Fused Filament Fabrication and Solvent Debinding: Selection of Binder Formulation. *Addit. Manuf.* **2019**, *26*, 117–128. [CrossRef]
29. McNulty, T.F.; Mohammadi, F.; Bandyopadhyay, A.; Shanefield, D.J.; Danforth, S.C.; Safari, A. Development of a Binder Formulation for Fused Deposition of Ceramics. *Rapid Prototyp. J.* **1998**, *4*, 144–150. [CrossRef]
30. Cano, S.; Gooneie, A.; Kukla, C.; Rieb, G.; Holzer, C.; Gonzalez-Gutierrez, J. Modification of Interfacial Interactions in Ceramic-Polymer Nanocomposites by Grafting: Morphology and Properties for Powder Injection Molding and Additive Manufacturing. *Appl. Sci.* **2020**, *10*, 1471. [CrossRef]
31. Momeni, V.; Shahroodi, Z.; Gonzalez-Gutierrez, J.; Hentschel, L.; Duretek, I.; Schuschnigg, S.; Kukla, C.; Holzer, C. Effects of Different Polypropylene (PP)-Backbones in Aluminium Feedstock for Fused Filament Fabrication (FFF). *Polymers* **2023**, *15*, 3007. [CrossRef]
32. Lengauer, W.; Duretek, I.; Fürst, M.; Schwarz, V.; Gonzalez-Gutierrez, J.; Schuschnigg, S.; Kukla, C.; Kitzmantel, M.; Neubauer, E.; Lieberwirth, C.; et al. Fabrication and Properties of Extrusion-Based 3D-Printed Hardmetal and Cermet Components. *Int. J. Refract. Met. Hard Mater.* **2019**, *82*, 141–149. [CrossRef]
33. Agarwala, M.K.; Jamalabad, V.R.; Langrana, N.A.; Safari, A.; Whalen, P.J.; Danforth, S.C. Structural Quality of Parts Processed by Fused Deposition. *Rapid Prototyp. J.* **1996**, *2*, 4–19. [CrossRef]
34. Agarwala, M.K.; van Weeren, R.; Bandyopadhyayl, A.; Whalen, P.J.; Safari, A.; Danforth, S.C. Fused Deposition of Ceramics and Metals: An Overview. In Proceedings of the Seventh Solid Freeform Fabrication Symposium, Austin, TX, USA, 12–14 August 1996; pp. 385–392.
35. Fayyaz, A.; Muhamad, N.; Sulong, A.B.; Yunn, H.S.; Amin, S.Y.M.; Rajabi, J. Micro-Powder Injection Molding of Cemented Tungsten Carbide: Feedstock Preparation and Properties. *Ceram. Int.* **2015**, *41*, 3605–3612. [CrossRef]
36. Yang, M.J.; German, R.M. Nanophase and Superfine Cemented Carbides Processed by Powder Injection Molding. *Int. J. Refract. Met. Hard Mater.* **1998**, *16*, 107–117. [CrossRef]
37. Percoco, G.; Arleo, L.; Stano, G.; Bottiglione, F. Analytical Model to Predict the Extrusion Force as a Function of the Layer Height, in Extrusion Based 3D Printing. *Addit. Manuf.* **2021**, *38*, 101791. [CrossRef]
38. Mbow, M.M.; Marin, P.R.; Pourroy, F. Extruded Diameter Dependence on Temperature and Velocity in the Fused Deposition Modeling Process. *Prog. Addit. Manuf.* **2020**, *5*, 139–152. [CrossRef]
39. Tarani, E.; Arvanitidis, I.; Christofilos, D.; Bikiaris, D.N.; Chrissafis, K.; Vourlias, G. Calculation of the Degree of Crystallinity of HDPE/GNPs Nanocomposites by Using Various Experimental Techniques: A Comparative Study. *J. Mater. Sci.* **2023**, *58*, 1621–1639. [CrossRef]
40. Wunderlich, B. *Thermal Analysis of Polymeric Materials*; Springer: Berlin/Heidelberg, Germany, 2005; ISBN 3-540-23629-5.
41. *ASTM B311-22*; Standard Test Method for Density Determination for Powder Metallurgy (P/M) Materials Containing Less Than Two Percent Porosity. ASTM International: West Conshohocken, PA, USA, 2022.
42. Gonzalez-Gutierrez, J.; Duretek, I.; Kukla, C.; Poljšak, A.; Bek, M.; Emri, I.; Holzer, C. Models to Predict the Viscosity of Metal Injection Molding Feedstock Materials as Function of Their Formulation. *Metals* **2016**, *6*, 129. [CrossRef]
43. Singh, P.; Balla, V.K.; Tofangchi, A.; Atre, S.V.; Kate, K.H. Printability Studies of Ti-6Al-4V by Metal Fused Filament Fabrication (MF3). *Int. J. Refract. Met. Hard Mater.* **2020**, *91*, 105249. [CrossRef]
44. Ghasemi-Mobarakeh, L.; Cano, S.; Momeni, V.; Liu, D.; Duretek, I.; Riess, G.; Kukla, C.; Holzer, C. Effect of Increased Powder–Binder Adhesion by Backbone Grafting on the Properties of Feedstocks for Ceramic Injection Molding. *Polymers* **2022**, *14*, 3653. [CrossRef]
45. Hwang, K.S. *Common Defects in Metal Injection Molding (MIM)*; Woodhead Publishing Limited: Sawston, UK, 2012; ISBN 9780857096234.
46. Hsueh, M.H.; Lai, C.J.; Wang, S.H.; Zeng, Y.S.; Hsieh, C.H.; Pan, C.Y.; Huang, W.C. Effect of Printing Parameters on the Thermal and Mechanical Properties of 3D-Printed Pla and Petg, Using Fused Deposition Modeling. *Polymers* **2021**, *13*, 1758. [CrossRef]
47. Heaney, D.F. Designing for Metal Injection Molding (MIM). *Handb. Met. Inject. Molding* **2012**, 29–49. [CrossRef]
48. Enneti, R.K.; Park, S.J.; German, R.M.; Atre, S.V. Review: Thermal Debinding Process in Particulate Materials Processing. *Mater. Manuf. Process.* **2012**, *27*, 103–118. [CrossRef]
49. Lotfizarei, Z.; Mostafapour, A.; Barari, A.; Jalili, A.; Patterson, A.E. Overview of Debinding Methods for Parts Manufactured Using Powder Material Extrusion. *Addit. Manuf.* **2023**, *61*, 103335. [CrossRef]
50. *ASTM B276-21*; Standard Test Method for Apparent Porosity in Cemented Carbides. ASTM International: West Conshohocken, PA, USA, 2021; pp. 1–19. [CrossRef]
51. German, R.M.; Suri, P.; Park, S.J. Review: Liquid Phase Sintering. *J. Mater. Sci.* **2009**, *44*, 1–39. [CrossRef]
52. García, J.; Collado Ciprés, V.; Blomqvist, A.; Kaplan, B. Cemented Carbide Microstructures: A Review. *Int. J. Refract. Met. Hard Mater.* **2019**, *80*, 40–68. [CrossRef]